Desalination and Water Treatment
www.deswater.com

doi: 10.1080/19443994.2015.1040851

57 (2016) 10745–10756
May

Taylor & Francis
Taylor & Francis Group

Facile preparation of mesoporous silica/nano zero-valent iron composite for Pb(II) removal from aqueous solution

Hongfei Lu, Xueliang Qiao*, Wei Wang, Fatang Tan, Zunqi Xiao, Jianguo Chen

State Key Laboratory of Material Processing and Die & Mould Technology, Huazhong University of Science and Technology, Wuhan 430074, P.R. China, Tel./Fax: +86 27 87541540; emails: 315079006@qq.com (H. Lu), hflu2011@163.com (X. Qiao), weiwang@hust.edu.cn (W. Wang), fatangtan@hust.edu.cn (F. Tan), 364884637@qq.com (Z. Xiao), jgchen5711@163.com (J. Chen)

Received 26 August 2014; Accepted 8 April 2015

ABSTRACT

Nano zero-valent iron (NZVI) particles were prone to forming aggregates owing to their intrinsic magnetism and van der Waals force. In this work, a composite material containing mesoporous silica MCM-41 and NZVI was prepared to avoid the problem of NZVI aggregation. The structures and morphologies of the as-prepared composite were confirmed using X-ray diffraction, Fourier transform infrared spectrometry, transmission electron microscopy, N_2 adsorption–desorption, and X-ray photoelectron spectroscopy techniques. It was found that NZVI particles were well dispersed in the composite, although the size of NZVI particle was larger than that of bare NZVI. Moreover, the composite was used as adsorbent for removing Pb(II) from aqueous solution at room temperature. The effects of contact time, initial solution pH, and adsorbent dosage on the removal efficiency of Pb(II) were studied using batch adsorption experiments. The results indicated the composite exhibited enhanced adsorption properties, with the maximum adsorption capacity of 416.17 mg/g for Pb(II) removal from aqueous solution. In addition, the adsorption isotherms and adsorption kinetics were also investigated systematically, it was found that the isothermal data were well fitted to Langmuir model, and the kinetic data were well suitable to pseudo-second-order kinetics model.

Keywords: Nano zero-valent iron; MCM-41; Adsorption; Lead ion

1. Introduction

Heavy metals pollution has become a serious environmental problem all over the world in recent years [1,2]. Among these heavy metal, Pb(II) is intensively concerned due to its high toxicity and tendency to accumulate in tissues of living organisms. Hence, it is very important to develop an effective method to remove Pb(II) from aqueous solution. Adsorption technique is widely used for the Pb(II) removal from wastewater due to its low cost, simplicity, and high efficiency [3,4]. Recently, nano zero-valent iron (NZVI) has been increasingly used for water remediation because of the advantages of high activity and absence of secondary pollution [5–7]. However, there are still some technical problems associated with practical applications, for example, the low stability and aggregation of NZVI particles [8]. Therefore, many attempts have been made to enhance the stability and the dispersity of NZVI [9,10].

*Corresponding author.

1944-3994/1944-3986 © 2015 Balaban Desalination Publications. All rights reserved.

Since 1992, mesoporous silica materials have attracted a great deal of attention due to their high-specific surface areas and size-tunable mesopores [11]. Silica-based inorganic–organic hybrid materials have been widely studied for removal of heavy metals [12–14]. Mesoporous silica materials modified with amino or thiol functional groups are promising adsorbents, which exhibit specific adsorption properties and larger adsorption capacity towards heavy metals [15,16]. However, it is necessary to use a large excess of organics during the synthesized process. Moreover, MCM-41 is an excellent mesoporous silica material, which presents large surface area, high physical–chemical stability, and well-defined pore size. There are many reports about using MCM-41 to prepare inorganic–inorganic composite material, such as, Ag/MCM-41 [17], Au/MCM-41 [18], and Mn_2O_3/MCM-41 [19]. However, to the best of our knowledge, MCM-41/NZVI composite material has been rarely reported.

In this work, a new composite material containing mesoporous silica MCM-41 and NZVI (MSNZVI) was synthesized and characterized by X-ray diffraction (XRD), Fourier transform infrared spectrometry (FTIR), N_2 adsorption–desorption, transmission electron microscopy (TEM), and X-ray photoelectron spectroscopy (XPS). The adsorption properties of the as-synthesized composite for removal of Pb(II) from aqueous solution was studied systematically. Also, the mechanism of removal of Pb(II) was proposed.

2. Materials and methods

2.1. Materials

All reagents were used in their analytical grade without further purification. Tetraethoxysilane (TEOS) 98%, ferrous sulfate heptahydrate ($FeSO_4{\cdot}7H_2O$) 99%, sodium chloride (NaCl) 99%, cetyltrimethylammonium bromide (CTAB) 98%, sodium borohydride ($NaBH_4$) 96%, sodium hydroxide (NaOH), lead nitrate $Pb(NO_3)_2$ 99%, and ethanol absolute, were purchased from Sinopharm Chemical Regent Co., Ltd. The stock solution containing 1,000 mg/L of Pb(II) was prepared by dissolving appropriate amount of $Pb(NO_3)_2$ into distilled water, and the solution pH was adjusted using 1.0 mol/L hydrochloric acid (HCl) and 1.0 mol/L sodium hydroxide (NaOH) solutions.

2.2. Preparation of bare NZVI, MCM-41 and MSNZVI

Bare NZVI was prepared by reducing $FeSO_4{\cdot}7H_2O$ with $NaBH_4$ in aqueous solution. Initially, 2.78 g of $FeSO_4{\cdot}7H_2O$ was dissolved into 50 mL of distilled water while stirring for 30 min. Then, 50 mL of freshly prepared aqueous solution containing 1.14 g of $NaBH_4$ was added dropwise into the above solution. The mixture was stirred for another 10 min. The black slurry was collected by magnetism and washed by deoxygenated water, absolute ethanol, and acetone, respectively. The whole process was carried out in an argon atmosphere. The reaction can be written as follows,

$$Fe^{2+} + 2BH_4^- + 6H_2O \rightarrow Fe^0 + 2B(OH)_3 + 7H_2 \uparrow \quad (1)$$

Mesoporous silica MCM-41 was prepared according to the method of Cai et al. [20]. Firstly, 0.7 mL of NaOH solution (2 M) was mixed with 100 mL of distilled water. Then, 0.2 g of CTAB was added to the solution while stirring at 80°C. When the solution became homogeneous, 1 mL of TEOS was added slowly. After 2 h, the resulting product was filtered, washed with distilled water, dried at 50°C, and calcined at 550°C for 4 h.

The preparation procedure for MSNZVI was as follows: 0.56 g of the as-prepared MCM-41 was added into 50 mL of distilled water and dispersed by ultrasonication. Then, 2.78 g of $FeSO_4{\cdot}7H_2O$ was added into the above solution under an argon atmosphere. After the mixture solution was stirred for 30 min, 50 mL of aqueous solution containing 1.14 g of $NaBH_4$ was added dropwise. The mixture solution was stirred for another 10 min. The solid product was separated by magnetism and washed by deoxygenated water, absolute ethanol, and acetone, respectively. The final product was dried under vacuum conditions and preserved under an argon atmosphere.

2.3. Characterization of MCM-41 and MSNZVI

XRD patterns were recorded on a Philips X'Pert PRO diffractometer, equipped with the Cu-Kα radiation and the accelerating voltage of 40 kV, emission current of 40 mA. TEM images were recorded on a JEOL JEM-100CX II TEM operating at an accelerating voltage of 100 kV. Infrared (IR) spectra were obtained on a Bruker VERTEX 70 FT-IR spectrophotometer in KBr pellets in the 4,000–400 cm^{-1} region. The N_2 adsorption–desorption isotherms were determined on a Micromertics ASAP 2020 V4.00 volumetric adsorption analyzer at 77 K. The specific surface area (S_{BET}) was estimated by the BET equation, and the pore size distribution was obtained from the Barrett–Joyner–Halenda (BJH) method. Surface composition of the samples was analyzed by X-ray photoelectron spectroscopy (XPS Kratos AXIS-ULTRA DLD with a monochromatic Al X-ray source at 130 W). Zero potential points were determined using a zeta potential analyzer (Brookhaven Zeta Plus, New York, USA).

2.4. Batch adsorption experiments

The adsorption of Pb(II) from aqueous solution was investigated in batch experiments. All of the mixture solutions were shaken at 250 rpm for 24 h using a thermostatic shaker at room temperature.

2.4.1. Effect of contact time

To study the effect of contact time, 480 mg of MSNZVI was added into 200 mL of Pb(II) solution with the concentration of 1,000 mg/L. The mixture solution was agitated in a shaker at room temperature, and 1 mL of sample was taken out at certain time intervals.

2.4.2. Effect of adsorbent dosage

To study the effect of adsorbent dosage, a series of 25 mL of Pb(II) solutions with the concentration of 1,000 mg/L were added into 50 mL Erlenmeyer flasks. The amount of MSNZVI was added varying from 15 to 90 mg. The mixture solutions were agitated in a shaker at room temperature for 24 h.

2.4.3. Effect of initial solution pH

The effect of initial solution pH on the adsorption of Pb(II) was investigated by mixing 60 mg of MSNZVI with 25 mL of Pb(II) stock solution. The pH values of solutions were adjusted to the desired values (2, 3, 4, 5, and 6) using 1.0 mol/L HCl or 1.0 mol/L NaOH solutions.

2.4.4. Adsorption kinetics

To study the adsorption kinetics, 200 mL of Pb(II) solutions with the concentration of 1,000 mg/L was firstly added into a 500 mL Erlenmeyer flask. Then, 480 mg of MSNZVI was added into the above solution. The mixture solution was agitated in a shaker at room temperature. Samples were taken out at certain time intervals. The adsorption kinetics was investigated according to the pseudo-first-order and the pseudo-second-order kinetics models.

2.4.5. Adsorption isotherms

A series of 25 mL of Pb(II) solutions with the concentrations of 50, 100, 200, 400, 600, 800, and 1,000 mg/L were added into 50 mL Erlenmeyer flasks, respectively. Then, 30 mg of MSNZVI was added into the above solutions. The mixture solutions were agitated in a shaker at room temperature for 24 h. Langmuir and Freundlich adsorption isotherm models were used to evaluate the adsorption equilibrium data.

For each test, samples were extracted and filtered by 0.25 μm filter membrane. The Pb(II) concentration of filtrates were determined by voltammetric analysis system (VAS, UK PDV6000 plus). The removal efficiency of Pb(II) and the adsorbed amount of MSNZVI were calculated by the following Eqs. (2) and (3), respectively.

$$\text{Removal } (\%) = \frac{(C_0 - C_t)}{C_0} \times 100 \tag{2}$$

$$q_t = \frac{(C_0 - C_t)V}{m} \tag{3}$$

where C_0 and C_t (mg/L) are the metal ions concentration in solution at the initial and at any time t, respectively; m (g) is the weight of MSNZVI, V (mL) is the volume of the solution, and q_t is the adsorption amount of MSNZVI at any time t.

3. Results and discussion

3.1. Characterization of MCM-41 and MSNZVI

The low-angle XRD pattern of MCM-41 is shown in Fig. 1(a). It indicated that MCM-41 possessed a typical hexagonal mesophase structure with a clear peak (1 0 0) and two weaker reflections assignable to (1 1 0) and (2 0 0) reflections [21]. The N_2 adsorption–desorption experimental isotherms at 77 K as well as the calculated pore size distribution of MCM-41 are plotted in Fig. 1(b). As seen in Fig. 1(b), the adsorption–desorption curve was type IV, which indicated the as-prepared MCM-41 was mesoporous nature [22]. Furthermore, the pore size distribution of the obtained MCM-41 with high-specific surface area of 744.27 m^2/g was mainly in the range of 2–4 nm, which was further confirmed that MCM-41 possessed mesoporous structure.

Fig. 2(a) presents the XPS wide-scan survey of MSNZVI. The photoelectron peaks revealed that the sample consisted of iron, oxygen, and silicon. Detailed XPS survey for Fe 2p region is shown in Fig. 2(b). The photoelectron peaks at around 710 and 723 eV corresponded to the binding energies of $2p_{3/2}$ and $2p_{1/2}$ of oxidized iron ($Fe{-}O_\chi$). A feature peak at 706.8 eV corresponded to the binding energy of $2p_{3/2}$ of zero-valent iron (Fe^0) [23]. Fig. 2(c) shows the wide-angle XRD pattern of MSNZVI. The broad diffraction peak

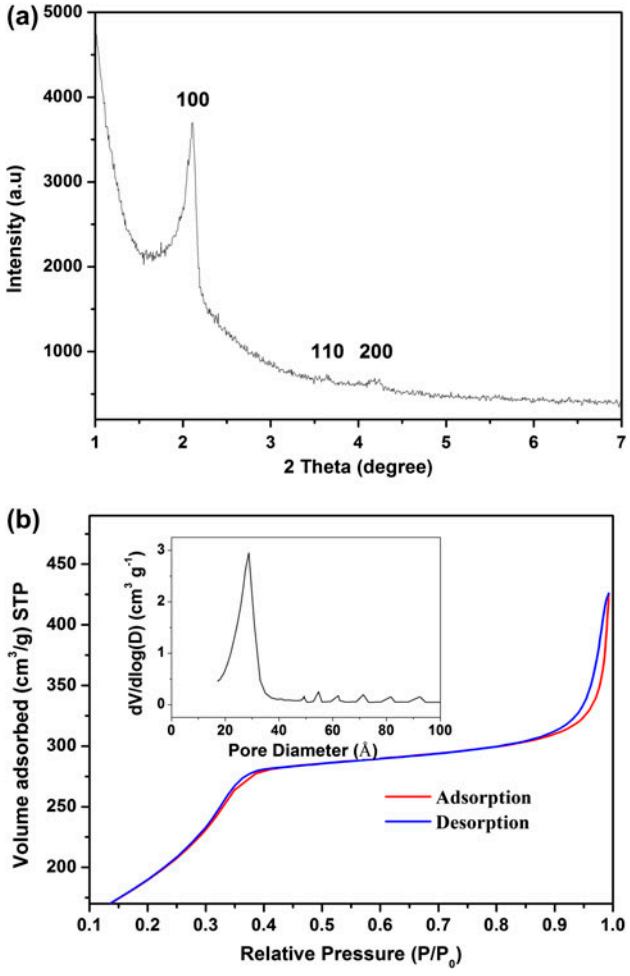

Fig. 1. (a) Low-angle XRD pattern of MCM-41 and (b) N_2 adsorption–desorption isotherm of MCM-41.

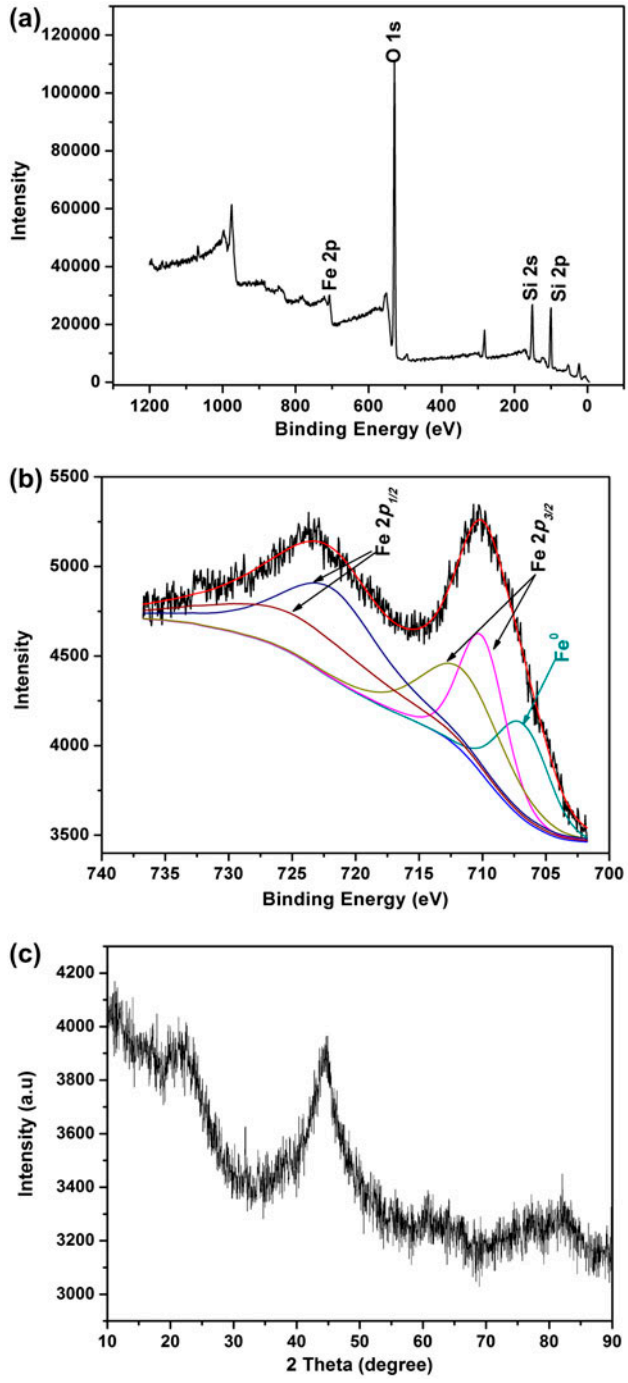

Fig. 2. (a) XPS wide-scan survey of MSNZVI, (b) detailed XPS survey of Fe 2p, and (c) wide-angle XRD pattern of MSNZVI.

around $2\theta = 21^\circ$ was ascribed to amorphous silica. The three broad diffraction peaks at $2\theta = 45^\circ$, 62°, and 82° can be assigned to the characteristic peaks of Fe^0 [24]. From the low-angle XRD pattern of MSNZVI shown in Fig. 3(a), it can be seen that the characteristic peaks of MCM-41 were disappeared, which indicated that the order pores of MCM-41 were filled with small NZVI particles. From the N_2 adsorption–desorption of MSNZVI (Fig. 3(b)), the specific surface area of MSNZVI was 247.41 m^2/g, which was much smaller than that of MCM-41. It could also indirectly prove that the pores of MCM-41 were filled with small NZVI particles.

The FTIR spectra of MCM-41 before calcination, MCM-41, and MSNZVI are shown in Fig. 4. The broad absorption band in the region 3,760−3,055 cm^{-1} was attributed to the stretching of Si−OH groups and the remaining physically adsorbed water molecules. The absorption bands at 1,080, 800, and 466 cm^{-1} were assigned to the Si–O–Si stretching [25]. The adsorption band at 1,639 cm^{-1} was due to bending of adsorbed water molecules. For MCM-41 before calcination, the adsorption peaks at 2,850, 2,930, and 1,480 cm^{-1} were found, which could be ascribed to the asymmetric

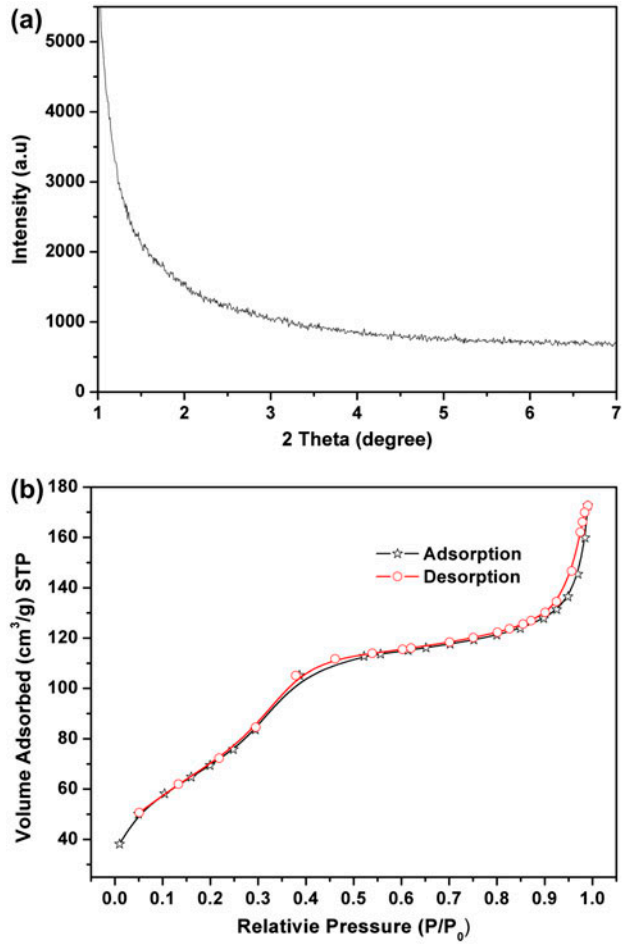

Fig. 3. (a) Low-angle XRD pattern of MSNZVI and (b) N_2 adsorption–desorption isotherm of MSNZVI.

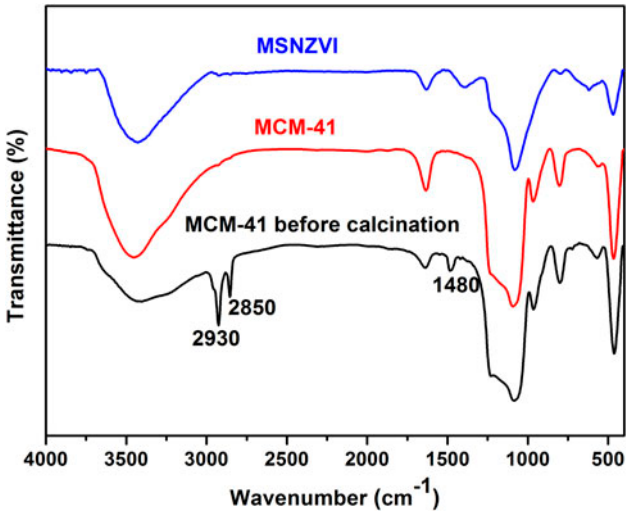

Fig. 4. FT-IR spectra of MCM-41 before calcination, MCM-41, and MSNZVI.

stretching, symmetric stretching, and bending of $-CH_2-$, respectively [26]. Apparently, these peaks were absent in the spectra of MCM-41 and MSNZVI, which revealed that CTAB was successfully removed from MCM-41 after calcination.

The representative TEM images of MCM-41, bare NZVI, and MSNZVI are illustrated in Fig. 5. As shown in Fig. 5(a), the particles of MCM-41 are near sphere or elongate sphere with size ranging from 80 to 100 nm. The sample possessed order 2D hexagonal mesophase and well-ordered pore arrangements, which was in consistent with XRD analysis of MCM-41. From Fig. 5(b), it can be seen that NZVI particles formed chain-like aggregates due to the strong van der Waals attraction as well as the magnetic interaction between the particles [27]. As shown in Fig. 5(c), the black spherical NZVI particles are well dispersed in the composite of MSNZVI, although the particle size was larger than that of the bare NZVI. It is observed from Fig. 5(d) that some small NZVI particles are adsorbed on the surface of MCM-41. Here, MCM-41 could be used as a dispersant for suppressing NZVI particles to form chain-like aggregates. In addition, MCM-41 could also provide crystal nuclei for promoting the growth of NZVI grains in the synthesis process of MSNZVI.

3.2. Adsorption studies

3.2.1. Effect of contact time

The effect of contact time on the adsorption of Pb (II) onto MSNZVI is shown in Fig. 6. It was observed that the adsorbed amount was increased from 208 to 392 mg/g with increasing contact time from 0.5 to 4 h. Pb(II) was adsorbed rapidly during the first 4 h, The rapid adsorption of Pb(II) in the initial stages was due to the increased in concentration gradient between the adsorbate in solution and the adsorbate in adsorbent [28]. After 6 h, the adsorbed amount did not change with further increase contact time, and the adsorption equilibrium time of Pb(II) onto MSNZVI was 6 h. In addition, the adsorption equilibrium was a dynamic-balanced process [29]. Therefore, 24 h selected as contact time for all of other experiments was deemed sufficient to ensure apparent equilibrium.

3.2.2. Effect of adsorbent dosage

The removal efficiency and the adsorbed amount for adsorption of Pb(II) onto MSNZVI with respect to MSNZVI dosage are shown in Fig. 7. The maximum adsorption capacity of MSNZVI was found to be 416.17 mg/g. The removal efficiency of Pb(II)

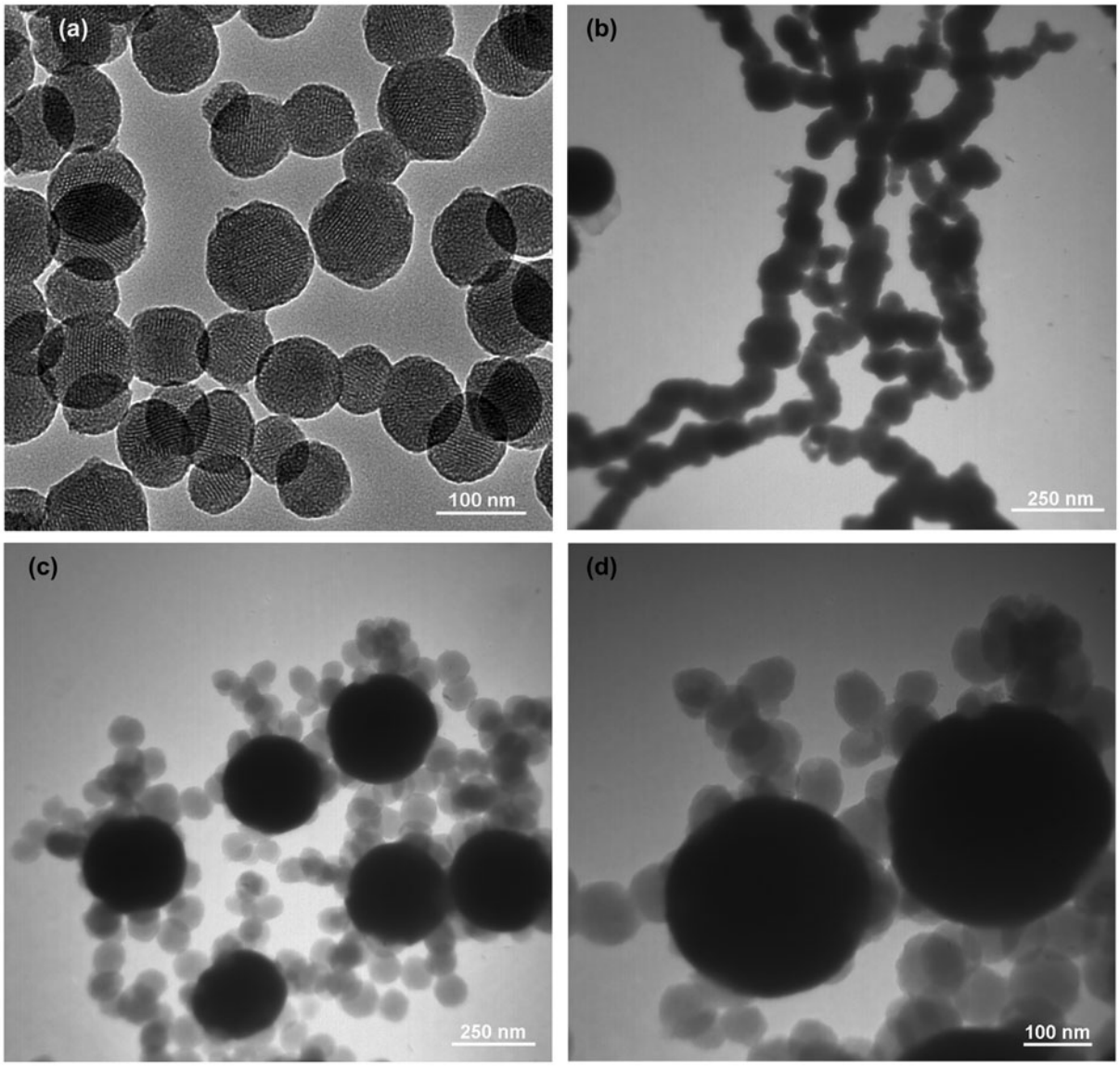

Fig. 5. TEM images of (a) MCM-41, (b) bare-NZVI, (c) MSNZVI, and (d) partial magnified image of MSNZVI.

increased with increasing MSNZVI dosage, whereas the adsorbed amount of per unit adsorbent was decreased with MSNZVI dosage increasing from 60 to 90 mg. These results can be explained that adsorbent surface was saturated with Pb(II) and the residual concentration of Pb(II) was large at low-adsorbent dosage. At higher adsorbent dosage, the adsorption sites were excessive for the demands of Pb(II) adsorption reaction, which leads to the unsaturation of the adsorption sites, resulting in comparatively less adsorption amount at higher adsorbent dosage [30].

The adsorption capacities of bare NZVI and MCM-41 for Pb(II) were also studied as control experiments in this paper. The results showed that the adsorption capacity of bare NZVI and MCM-41 was 319.24 and 39.06 mg/g, respectively. Obviously, the adsorption capacity of MSNZVI was higher than that of bare NZVI and pristine MCM-41. On the one hand, MCM-41 could be used as a dispersant in the MSNZVI composite, to enhance the dispersity of NZVI particles, which could result in an increase in specific surface area of NZVI. On the other hand, the small NZVI particles adsorbed on MCM-41 spheres could increase the adsorption active sites of MCM-41. Hence, the adsorption capacity of MSNZVI was improved due to the synergistic effect of NZVI and MCM-41.

In this work, the maximum adsorption capacity of MSNZVI for Pb(II) (416.17 mg/g) was higher than that of reported Sineguelas–NaOH–NZVI composite (225 mg/g) [31]. Although it was lower than that of

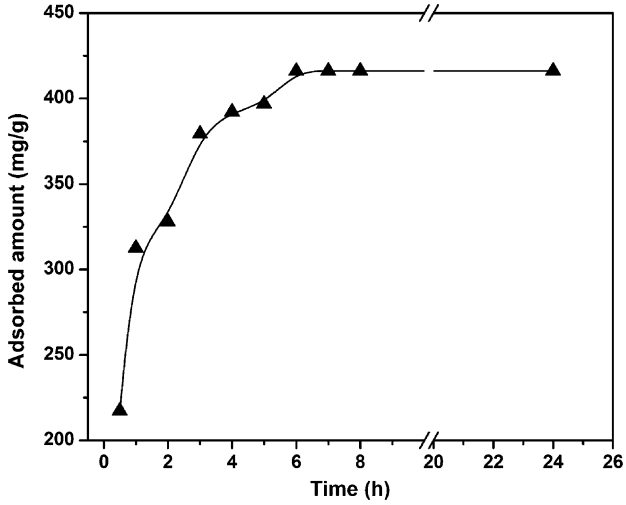

Fig. 6. Effect of contact time on Pb(II) adsorption (experimental conditions: T = 298 K; initial Pb(II) concentration = 1,000 mg/L; solution volume = 200 mL; pH 5; MSNZVI = 480 mg).

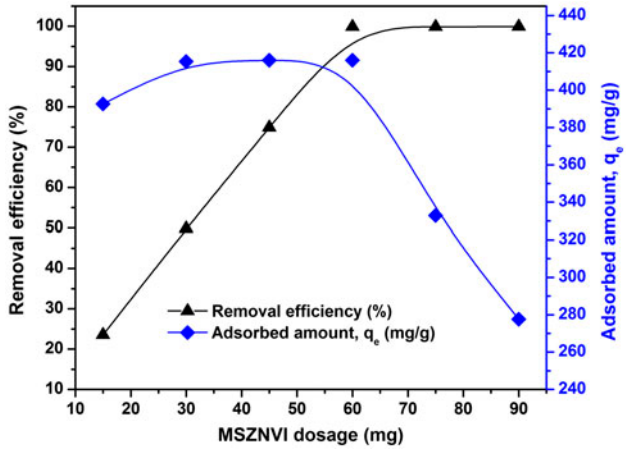

Fig. 7. Effect of adsorbent dosage on Pb(II) adsorption (experimental conditions: T = 298 K; initial Pb(II) concentration = 1,000 mg/L; solution volume = 25 mL; pH 5).

zero-valent iron nanoparticles–Graphene composite (555.6 mg/g) [32] and nano-graphite carbon-impregnated calcium alginate bead (460.9 mg/g) [33], but the cost of MCM-41 was lower and the synthetic process of MSNZVI was more facile than these composites. Therefore, MSNZVI has a potential application for removal of Pb(II) from aqueous solutions.

3.2.3. Effect of initial solution pH

Since the concentration of Pb(II) is 1,000 mg/L, it would generate insoluble species at pH > 6 according

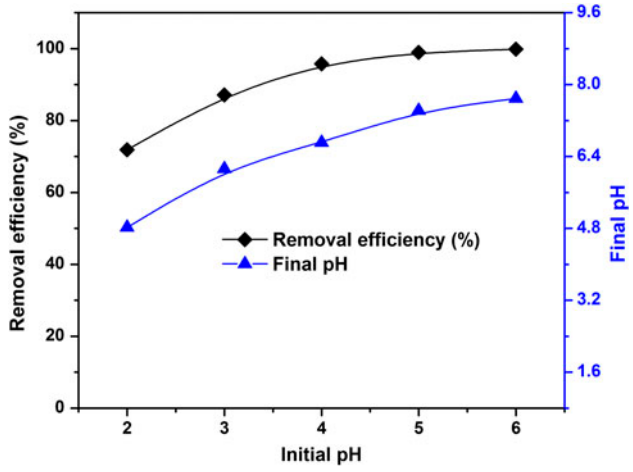

Fig. 8. Effect of initial solution pH on Pb(II) adsorption (experimental conditions: T = 298 K; initial Pb(II) concentration = 1,000 mg/L; solution volume = 25 mL; MSNZVI = 60 mg).

to the solubility product (K_{sp}) of $Pb(OH)_2$ at room temperature. Therefore, the pH range of 2.0–6.0 was selected for this study. As shown in Fig. 8, the removal efficiency of Pb(II) increased with the increasing initial solution pH. At a low solution pH, the concentration of the hydrogen ions was high, directly competing with Pb(II) for active binding site. Additionally, some NZVI particles reacted with hydrogen ions, which can inhibit the reduction reaction between Pb(II) and NZVI [34]. Therefore, the removal efficiency increased with the increasing solution pH. Furthermore, the zeta potential of MCM-41 and MSNZVI particles (1 g/L) as a function of pH is shown in Fig. 9, which is measured in 1 moL/L NaCl aqueous

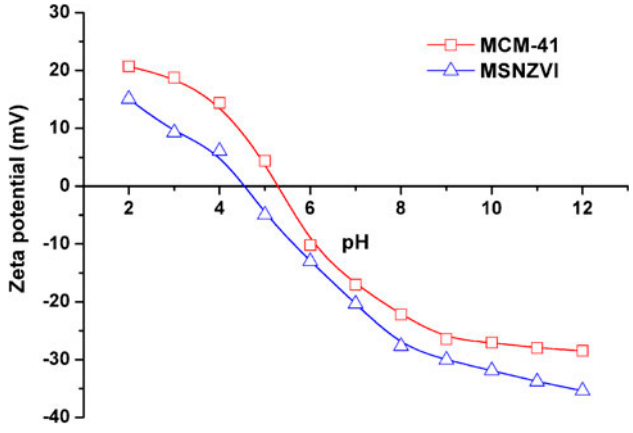

Fig. 9. Zeta potentials of (△) MSNZVI and (□) MCM-41 in 1 mmoL/L NaCl solution at varied pH values. Total concentration is 1 g/L.

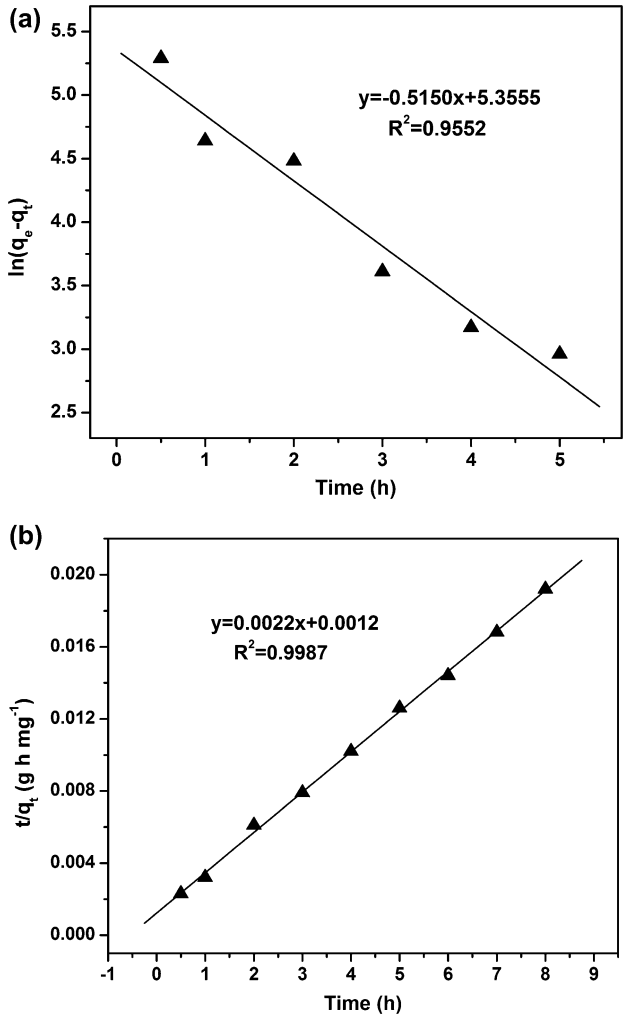

Fig. 10. Adsorption kinetics of Pb(II) onto MSNZVI (experimental conditions: T = 298 K; solution volume = 200 mL; pH 5; MSNZVI = 480 mg): (a) pseudo-first-order model plot and (b) pseudo-second-order model plot.

solutions at pH 2–12 (adjusted by NaOH or HCl). It can be seen that the zero potential points of MCM-41 and MSNZVI were about at pH 5.23 and 4.54, respectively. And the zeta potential exhibited negative charge when pH was higher than the zero potential points. Therefore, these could also confirm that the removal efficiency increased with increasing the solution pH.

In addition, the final pH value of solution was also studied. The results are shown in Fig. 8 (blue curve). It was observed that the final pH values of all solutions were increased, it may be because that NZVI reacted with water and oxide species to give Fe^{2+} and OH^- according to the Eqs. (4) and (5) [35].

$$2Fe^0 + 2H_2O \rightarrow 2Fe^{2+} + H_2 + 2OH^- \quad (4)$$

$$2Fe^0 + O_2 + 2H_2O \rightarrow 2Fe^{2+} + 4OH^- \quad (5)$$

3.2.4. Adsorption kinetics

The adsorption rate is an important parameter employed to evaluate the adsorption process. Pseudo-first-order and pseudo-second-order kinetic models were used to study the adsorption kinetics of Pb(II) [36]. The linear forms of these two models are expressed by the Eqs. (6) and (7), respectively.

$$\ln(q_e - q_t) = \ln q_e - k_1 t \quad (6)$$

$$\frac{t}{q_t} = \frac{1}{k_2 q_e^2} + \frac{1}{q_e} t \quad (7)$$

where q_e (mg/g) and q_t (mg/g) are the amounts of Pb (II) adsorbed onto the adsorbent at equilibrium and time t (h), respectively. k_1 (h^{-1}) and k_2 (mg g^{-1} h^{-1}) are the rate constants of the pseudo-first-order and the pseudo-second-order kinetic models, respectively.

According to the experimental data of adsorbed amount with respect to contact time (Fig. 6), the adsorption kinetics of Pb(II) is discussed using the pseudo-first-order and the pseudo-second-order kinetic models. The linear plots of $\ln(q_e - q_t)$ vs. t, and t/q_t vs. t are shown in Fig. 10(a) and (b), respectively, and the parameters of the two kinetic models are summarized in Table 1. The results showed the pseudo-second-order rate equation for adsorption of Pb(II) onto MSNZVI agreed well with the data for R^2 = 0.9987. In addition,

Table 1
Pseudo-first-order and pseudo-second-order kinetic parameters for adsorption of Pb(II) onto MSNZVI

		Pseudo-first-order			Pseudo-second-order		
Temp (K)	$q_{e,exp}$ (mg g^{-1})	k_1 (h^{-1})	$q_{e,cal}$ (mg g^{-1})	R^2	k_2 (g mg^{-1} h^{-1})	$q_{e,cal}$ (mg g^{-1})	R^2
298	416.17	0.5150	211.77	0.9552	0.0040	454.55	0.9987

the calculated adsorption capacity value ($q_{e(cal)}$) obtained from pseudo-second-order model was more closer to the experimental value of adsorption capacity ($q_{e(exp)}$). Therefore, the pseudo-second-order model was better fitted with the adsorption kinetics of Pb(II) onto MSNZVI in contrast to the pseudo-first-order model [37].

3.2.5. Adsorption isotherms

In order to predict the adsorption behavior of Pb (II) onto MSNZVI, Langmuir and Freundlich adsorption isotherm models were used to interpret the adsorption equilibrium experimental data. The linear forms of these two adsorption isotherm models are represented by Eqs. (8) and (9) [38], respectively.

$$\frac{C_e}{q_e} = \frac{1}{K_L q_m} + \frac{C_e}{q_m} \tag{8}$$

$$\ln q_e = \ln K_F + \frac{1}{n} \ln C_e \tag{9}$$

where q_e (mg/g) is the amount of Pb(II) adsorbed at equilibrium, C_e (mg/L) is equilibrium concentration of Pb(II) in solution, q_m (mg/g) is the maximum adsorption capacity of adsorbent, K_L (L/mg) is the Langmuir constant, K_F ($mg^{1-1/n}\,L^{1/n}\,g^{-1}$) is the Freundlich constant, and n is the Freundlich constant related to the adsorption intensity of adsorption.

Moreover, as Eq. (10) shown, the value of R_L is a dimensionless constant, which can indicate whether the type of Langmuir isotherm is favorable ($0 < R_L < 1$), unfavorable ($R_L > 1$) or irreversible ($R_L = 0$) [39].

$$R_L = \frac{1}{1 + K_L C_0} \tag{10}$$

The adsorption equilibrium studies of Pb(II) were carried out varying the concentration from 50 to 1,000 mg/L, the adsorption equilibrium plot is shown in Fig. 11(a). On the basis of this profile, the linear plots of $\ln q_e$ vs. $\ln c_e$, and c_e/q_e vs. c_e are presented in Fig. 11(b) and (c), respectively, and the parameters of the two adsorption models are also listed in Table 2. The linear correlation coefficient value of Langmuir model was 0.9997, and the calculated adsorption capacity value (q_m) obtained from Langmuir model was more consistent with the experimental value of adsorption capacity ($q_{e(exp)}$). Hence, Langmuir model fitted the experimental data better in contrast to

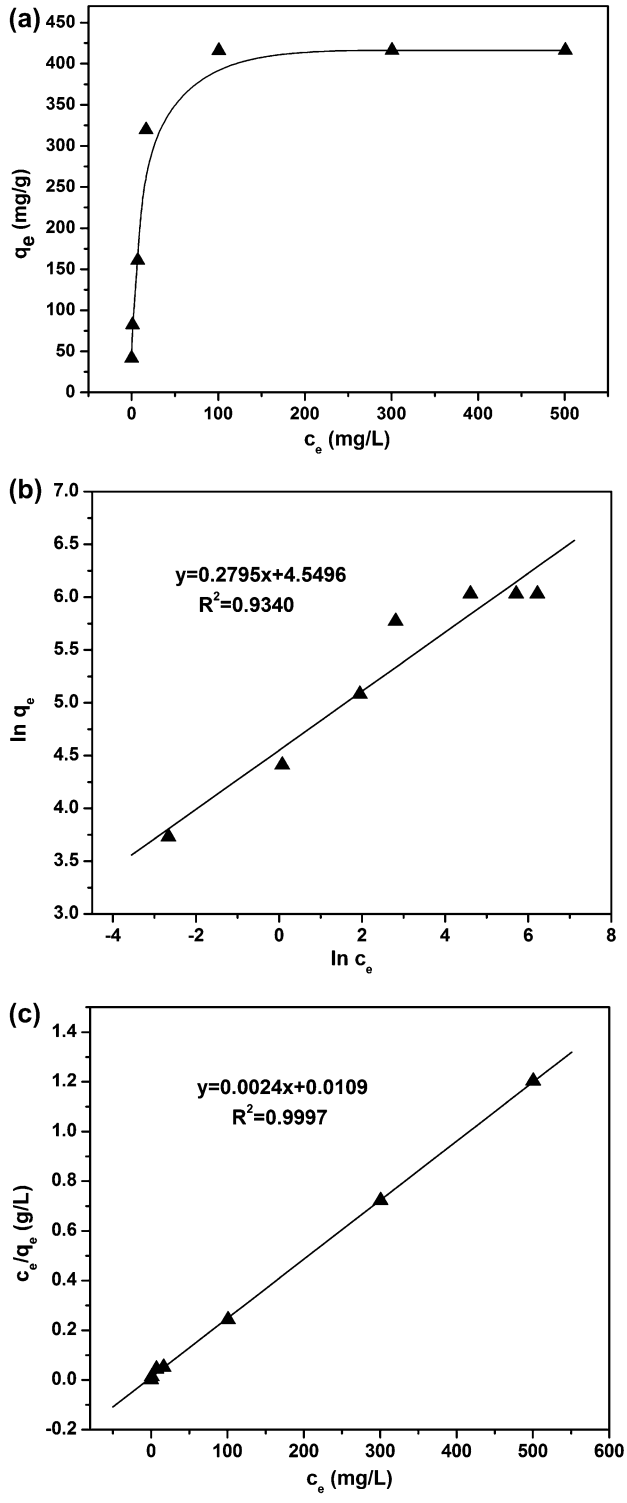

Fig. 11. Adsorption isotherms of Pb(II) onto MSNZVI (experimental conditions: T = 298 K; solution volume = 25 mL; pH 5; MSNZVI = 30 mg): (a) equilibrium adsorption isotherms of Pb(II) onto MSNZVI; (b) Freundlich isotherm model plot; and (c) Langmuir isotherm model plot.

Table 2
Langmuir and Freundlich parameters for adsorption of Pb(II) onto MSNZVI

	Langmuir model				Freundlich model		
Temp (K)	q_m (mg g^{-1})	K_L (L mg^{-1})	R^2	R_L	K_F ($mg^{1-1/n}$ $L^{1/n}$ g^{-1})	n	R^2
298	416.67	0.22	0.9997	0.0833–0.0045	94.59	3.58	0.9340

Freundlich model. Furthermore, the value of R_L for the Langmuir isotherm was between 0 and 1, and the Freundlich constant $1/n$ was smaller than 1, which also suggested that the adsorption of Pb(II) onto MSNZVI was fitted well with the Langmuir model.

3.2.6. Possible mechanism of Pb(II) removal

Previous studies indicate that NZVI particles typically have a core-shell structure with the core being zero-valent iron (Fe^0) and the shell being the iron oxides/hydroxides [40,41]. This structure presented NZVI with unique performance for heavy metal ions removal. The possible mechanism of Pb(II) removal using MSNZVI from aqueous solution should include both adsorption and reduction processes. Firstly, the NZVI particles had the core-shell structure with the shell as the iron oxides/hydroxides, which had many hydroxyl groups from the surface of NZVI particles, and there were many hydroxyl groups from the MCM-41 particles. These hydroxyl groups provided many bind sites for the adsorption of Pb(II). Fig. 12(a) shows the XPS survey scan of MSNZVI after the adsorption of Pb(II). The photoelectron peaks revealed that particles surface consisted of iron, oxygen, silicon, and lead. It was indicated that Pb(II) was adsorbed onto the surface of MSNZVI particles. Secondly, the detailed XPS survey of Pb 4f is shown in Fig. 12(b). The photoelectron peaks at around 138.7 and 143.5 eV could be assigned to Pb(II) binding energies for $4f_{7/2}$ and $4f_{5/2}$ orbital, respectively [42]. However, the 4f peak of Pb^0 at about 136.6 eV was not detected, which was similar to Ponder and Zhang's reports [43,44]. It was unclear whether the presence of surface Pb(II) resulted from the adsorption of Pb(II) from the solution or the oxidation of the possible Pb^0 formed in the reaction. But, the redox mechanism of Pb(II) by Fe^0 was justified by the fact that the standard oxidation–reduction potential (E^0) of the Pb^{2+}/Pb^0 (−0.13 V) was more positive than that of Fe^{2+}/Fe^0 (−0.41 V) [40]. Hence, it could be inferred that there exist the reduction of Pb(II) by Fe^0.

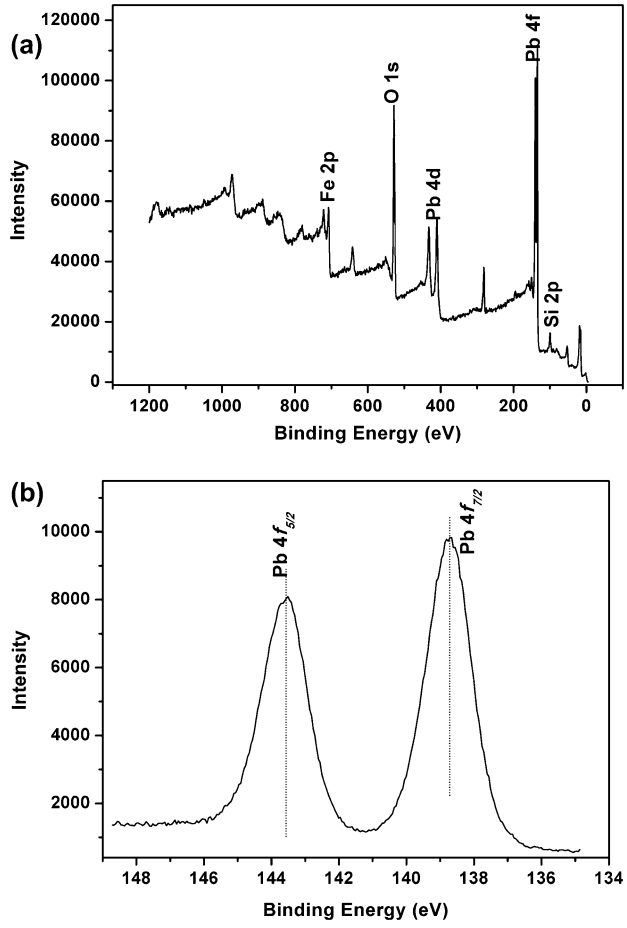

Fig. 12. (a) XPS wide-scan survey of MSNZVI after Pb(II) treatment and (b) detailed XPS survey of Pb 4f.

4. Conclusions

In the present study, mesoporous silica MCM-41/NZVI composite (MSNZVI) was facilely prepared and systematically characterized. The NZVI particles were well dispersed in the MSNZVI composite. The adsorption performances of the MSNZVI composite for Pb(II) were studied systematically. The results of adsorption experiments demonstrated that the adsorption capacity

of MSNZVI composite for Pb(II) (416.17 mg/g) was higher than those of bare NZVI (319.24 mg/g) and pristine MCM-41 (39.06 mg/g), which could be attributed to the synergistic effect of NZVI and MCM-41. Moreover, the adsorption process of Pb(II) onto MSNZVI composite was found to well obey the pseudo-second-order kinetic model and Langmuir adsorption model. Additionally, the mechanism of Pb (II) removal using MSNZVI composite involving adsorption and reduction was proposed and confirmed. All of these results suggest that MSNZVI composite has the potential application for Pb(II) removal from aqueous solution.

Acknowledgments

The authors thank the Analysis and Test center of HUST (Huazhong University of Science and Technology) for providing the research facilities.

References

[1] A. Heidari, H. Younesi, Z. Mehraban, Removal of Ni (II), Cd(II), and Pb(II) from a ternary aqueous solution by amino functionalized mesoporous and nano mesoporous silica, Chem. Eng. J. 153 (2009) 70–79.
[2] D.A. Grassi, M. Galicio, A. Fernández Cirelli, A homogeneous and low-cost biosorbent for Cd, Pb and Cu removal from aqueous effluents, Chem. Ecol. 27 (2011) 297–309.
[3] P. Kumar, R. Rao, S. Chand, S. Kumar, K. Wasewar, C.K. Yoo, Adsorption of lead from aqueous solution onto coir-pith activated carbon, Desalin. Water Treat. 51 (2013) 2529–2535.
[4] M. Medina, J. Tapia, S. Pacheco, M. Espinosa, R. Rodriguez, Adsorption of lead ions in aqueous solution using silica–alumina nanoparticles, J. Non-Cryst. Solids. 356 (2010) 383–387.
[5] A.B. Cundy, L. Hopkinson, R.L. Whitby, Use of iron-based technologies in contaminated land and groundwater remediation: A review, Sci. Total Environ. 400 (2008) 42–51.
[6] M.-K. Ji, Y.-T. Ahn, M. Ali Khan, R.A. Abou-Shanab, Y. Cho, J.-Y. Choi, Y. Je Kim, H. Song, B.-H. Jeon, Removal of nitrate and ammonium ions from livestock wastewater by hybrid systems composed of zero-valent iron and adsorbents, Environ. Technol. 32 (2011) 1851–1857.
[7] C.M. Rogers, I.T. Burke, I.A. Ahmed, S. Shaw, Immobilization of chromate in hyperalkaline waste streams by green rusts and zero-valent iron, Environ. Technol. 35 (2014) 508–513.
[8] J. Zhan, T. Zheng, G. Piringer, C. Day, G.L. McPherson, Y. Lu, K. Papadopoulos, V.T. John, Transport characteristics of nanoscale functional zerovalent iron/silica composites for *in situ* remediation of trichloroethylene, Environ. Sci. Technol. 42 (2008) 8871–8876.
[9] A. Gupta, M. Yunus, N. Sankararamakrishnan, Zerovalent iron encapsulated chitosan nanospheres—A novel adsorbent for the removal of total inorganic Arsenic from aqueous systems, Chemosphere 86 (2012) 150–155.
[10] F. He, D. Zhao, Manipulating the size and dispersibility of zerovalent iron nanoparticles by use of carboxymethyl cellulose stabilizers, Environ. Sci. Technol. 41 (2007) 6216–6221.
[11] C. Kresge, M. Leonowicz, W. Roth, J. Vartuli, J. Beck, Ordered mesoporous molecular sieves synthesized by a liquid-crystal template mechanism, Nature 359 (1992) 710–712.
[12] F.-K. Shieh, C.-T. Hsiao, H.-M. Kao, Y.-C. Sue, K.-W. Lin, C.-C. Wu, X.-H. Chen, L. Wan, M.-H. Hsu, J.R. Hwu, Size-adjustable annular ring-functionalized mesoporous silica as effective and selective adsorbents for heavy metal ions, RSC Adv. 3 (2013) 25686–25689.
[13] P. Valle-Vigón, M. Sevilla, A.B. Fuertes, Carboxyl-functionalized mesoporous silica–carbon composites as highly efficient adsorbents in liquid phase, Micropor. Mesopor. Mater. 176 (2013) 78–85.
[14] G. Li, Z. Zhao, J. Liu, G. Jiang, Effective heavy metal removal from aqueous systems by thiol functionalized magnetic mesoporous silica, J. Hazard. Mater. 192 (2011) 277–283.
[15] M. Barczak, R. Dobrowolski, J. Dobrzyńska, E. Zięba, A. Dąbrowski, Amorphous and ordered organosilicas functionalized with amine groups as sorbents of platinum (II) ions, Adsorption 19 (2013) 733–744.
[16] J.M. Arsuaga, J. Aguado, A. Arencibia, M.S. López-Gutiérrez, Aqueous mercury adsorption in a fixed bed column of thiol functionalized mesoporous silica, Adsorption 20 (2014) 311–319.
[17] A. Yin, C. Wen, W.-L. Dai, K. Fan, Ag/MCM-41 as a highly efficient mesostructured catalyst for the chemoselective synthesis of methyl glycolate and ethylene glycol, Appl. Catal. B: Environ. 108–109 (2011) 90–99.
[18] A. Kumar, V.P. Kumar, V. Vishwanathan, K.V. Chary, Synthesis, characterization, and reactivity of Au/MCM-41 catalysts prepared by homogeneous deposition–precipitation (HDP) method for vapor phase oxidation of benzyl alcohol, Mater. Res. Bull. 61 (2015) 105–112.
[19] B. Han, F. Zhang, Z. Feng, S. Liu, S. Deng, Y. Wang, Y. Wang, A designed Mn_2O_3/MCM-41 nanoporous composite for methylene blue and rhodamine B removal with high efficiency, Ceram. Int. 40 (2014) 8093–8101.
[20] Q. Cai, Z.-S. Luo, W.-Q. Pang, Y.-W. Fan, X.-H. Chen, F.-Z. Cui, Dilute solution routes to various controllable morphologies of MCM-41 silica with a basic medium, Chem. Mater. 13 (2001) 258–263.
[21] S.A. Idris, C.M. Davidson, C. McManamon, M.A. Morris, P. Anderson, L.T. Gibson, Large pore diameter MCM-41 and its application for lead removal from aqueous media, J. Hazard. Mater. 185 (2011) 898–904.
[22] N. Wu, W. Zhang, B. Li, C. Han, Nickel nanoparticles highly dispersed with an ordered distribution in MCM-41 matrix as an efficient catalyst for hydrodechlorination of chlorobenzene, Micropor. Mesopor. Mater. 185 (2014) 130–136.

[23] Y.-H. Lin, H.-H. Tseng, M.-Y. Wey, M.-D. Lin, Characteristics of two types of stabilized nano zero-valent iron and transport in porous media, Sci. Total Environ. 408 (2010) 2260–2267.
[24] Y.c. Li, Z.h. Jin, T.l. Li, A novel and simple method to synthesize SiO_2-coated Fe nanocomposites with enhanced Cr (VI) removal under various experimental conditions, Desalination 288 (2012) 118–125.
[25] G. Grigoropoulou, P. Stathi, M. Karakassides, M. Louloudi, Y. Deligiannakis, Functionalized SiO_2 with N-, S-containing ligands for Pb(II) and Cd(II) adsorption, Colloid. Surf. A: Physicochem Eng Aspects. 320 (2008) 25–35.
[26] O. Yayapao, T. Thongtem, A. Phuruangrat, S. Thongtem, CTAB-assisted hydrothermal synthesis of tungsten oxide microflowers, J. Alloys Compd. 509 (2011) 2294–2299.
[27] N. Saleh, K. Sirk, Y. Liu, T. Phenrat, B. Dufour, K. Matyjaszewski, R.D. Tilton, G.V. Lowry, Surface modifications enhance nanoiron transport and NAPL targeting in saturated porous media, Environ. Eng. Sci. 24 (2007) 45–57.
[28] M.D. Meitei, M.N.V. Prasad, Lead (II) and cadmium (II) biosorption on Spirodela polyrhiza (L.) Schleiden biomass, J. Environ Chem. Eng. 1 (2013) 200–207.
[29] G. Tan, D. Xiao, Adsorption of cadmium ion from aqueous solution by ground wheat stems, J. Hazard. Mater. 164 (2009) 1359–1363.
[30] Q. Qin, Q. Wang, D. Fu, J. Ma, An efficient approach for Pb(II) and Cd(II) removal using manganese dioxide formed *in situ*, Chem. Eng. J. 172 (2011) 68–74.
[31] M. Arshadi, M. Soleymanzadeh, J. Salvacion, F. SalimiVahid, Nanoscale zero-valent iron (NZVI) supported on *sineguelas* waste for Pb(II) removal from aqueous solution: Kinetics, thermodynamic and mechanism, J. Colloid Interface Sci. 426 (2014) 241–251.
[32] H. Jabeen, K.C. Kemp, V. Chandra, Synthesis of nano zerovalent iron nanoparticles—Graphene composite for the treatment of lead contaminated water, J. Environ. Manage. 130 (2013) 429–435.
[33] D.-W. Cho, W. Jung, A. Sigdel, O.-H. Kwon, S.-H. Lee, A.N. Kabra, B.-H. Jeon, Adsorption of Pb(II) and Ni (II) from aqueous solution by nanosized graphite carbon-impregnated calcium alginate bead, Geosy. Eng. 16 (2013) 200–208.
[34] Y. Cheng, C. Jiao, W. Fan, Synthesis and characterization of coated zero-valent iron nanoparticles and their application for the removal of aqueous Pb^{2+} ions, Desalin. Water Treat. (2014) 1–9.
[35] S.R. Kanel, B. Manning, L. Charlet, H. Choi, Removal of arsenic(III) from groundwater by nanoscale zero-valent iron, Environ. Sci. Technol. 39 (2005) 1291–1298.
[36] V. Sarin, K. Pant, Removal of chromium from industrial waste by using eucalyptus bark, Bioresour. Technol. 97 (2006) 15–20.
[37] Y. Liu, Z. Liu, J. Gao, J. Dai, J. Han, Y. Wang, J. Xie, Y. Yan, Selective adsorption behavior of Pb(II) by mesoporous silica SBA-15-supported Pb(II)-imprinted polymer based on surface molecularly imprinting technique, J. Hazard. Mater. 186 (2011) 197–205.
[38] H.B. Bradl, Adsorption of heavy metal ions on soils and soils constituents, J. Colloid Interface Sci. 277 (2004) 1–18.
[39] S. Azizian, Kinetic models of sorption: A theoretical analysis, J. Colloid Interface Sci. 276 (2004) 47–52.
[40] X.-Q. Li, W.-X. Zhang, Sequestration of metal cations with zerovalent iron nanoparticles—A Study with high resolution X-ray photoelectron spectroscopy (HR-XPS), J. Phys. Chem. C 111 (2007) 6939–6946.
[41] Y. Zhang, Y. Su, X. Zhou, C. Dai, A.A. Keller, A new insight on the core–shell structure of zerovalent iron nanoparticles and its application for Pb(II) sequestration, J. Hazard. Mater. 263 (2013) 685–693.
[42] S. Luo, T. Lu, L. Peng, J. Shao, Q. Zeng, J.-D. Gu, Synthesis of nanoscale zero-valent iron immobilized in alginate microcapsules for removal of Pb(II) from aqueous solution, J. Mater. Chem. A 2 (2014) 15463–15472.
[43] S.M. Ponder, J.G. Darab, T.E. Mallouk, Remediation of Cr(VI) and Pb(II) aqueous solutions using supported, nanoscale zero-valent iron, Environ. Sci. Technol. 34 (2000) 2564–2569.
[44] X. Zhang, S. Lin, Z. Chen, M. Megharaj, R. Naidu, Kaolinite-supported nanoscale zero-valent iron for removal of Pb^{2+} from aqueous solution: Reactivity, characterization and mechanism, Water Res. 45 (2011) 3481–3488.